CHIN. PHYS. LETT. Vol. 35, No. 12 (2018) 127501

Magnetic and topological transitions in three-dimensional topological Kondo insulator *

Huan Li(黎欢)[1**], Zhi-Yong Wang(王志勇)[1], Xiao-Jun Zheng(郑晓军)[1**], Yu Liu(刘瑜)[2,3], Yin Zhong(钟寅)[4]

[1]College of Science, Guilin University of Technology, Guilin 541004
[2]Institute of Applied Physics and Computational Mathematics, Beijing 100088
[3]Software Center for High Performance Numerical Simulation, China Academy of Engineering Physics, Beijing 100088
[4]Center for Interdisciplinary Studies & Key Laboratory for Magnetism and Magnetic Materials of the MoE, Lanzhou University, Lanzhou 730000

(Received 26 September 2018)

Using an extended slave-boson method, we draw a global phase diagram summarizing both magnetic phases and paramagnetic (PM) topological insulators (TIs) in a three-dimensional topological Kondo insulator (TKI). By including electron hopping (EH) up to the third neighbors, we identify four strong TI (STI) phases and two weak TI (WTI) phases. Then, the PM phase diagrams characterizing topological transitions between these TIs are depicted as functions of EH, f-electron energy level, and hybridization constant. We also find an insulator–metal transition from an STI phase that has surface Fermi rings and spin textures in qualitative agreement with the TKI candidate SmB_6. In the weak hybridization regime, antiferromagnetic (AF) order naturally arises in the phase diagrams. Depending on how the magnetic boundary crosses the PM topological transition lines, AF phases are classified into the AF topological insulator (AFTI) and the non-topological AF insulator, according to their $\mathcal{Z}_2$ indices. In two small regions of parameter space, two distinct topological transition processes between AF phases occur, leading to two types of AFTIs showing distinguishable surface dispersions around their Dirac points.

PACS: 75.30.Mb, 75.30.Kz, 75.70.Tj DOI: 10.1088/0256-307X/35/12/127501

Over the recent years, searching topological phases of matter has become one of the central topics in condensed matter physics.[1] Among the enlarging family of topological materials, strongly correlated electron systems are taken as important bases because they naturally involve rich kinds of mechanisms, and hence can generate a variety of interacting topological phases. These include interacting topological insulators (TIs),[2] topological Mott insulators,[3] interacting topological superconductors,[4] Weyl semimetals,[5] topological Kondo insulators (TKIs),[6] and antiferromagnetic TIs (AFTIs).[7–10] The TKI,[6] a heavy-fermion system with strong Coulomb interaction and d–f hybridization governed by spin-orbit coupling, preserves time-reversal symmetry (TRS), and can therefore generate TIs with a Kondo screening effect. As revealed by previous works, a variation of electron hopping (EH) strength, f-electron energy level ϵ_f, and hybridization constant V can drive topological transitions among phases of strong TIs (STIs), weak TIs (WTIs), and normal Kondo insulators (nKIs).[11] However, the existing works are restricted to their interesting parameter regime. Hence, the studied TIs are still confined to a limited number of STIs and WTIs, and the full STI and WTI phases in TKIs have not been explored adequately, particularly in the presence of strong electron–electron correlation.[11] In this work, considering adequate parameter space of the periodic Anderson model (PAM), we uncover all possible TIs in the three-dimensional (3D) TKI: four STIs and two WTIs, each possessing distinct surface states and Dirac cones. We also present the paramagnetic (PM) phase diagrams characterizing topological transitions between these TIs as functions of EH, ϵ_f, and V. By proper fitting of EH, we verify an STI phase with Fermi surfaces and spin textures that can qualitatively simulate the TKI material SmB_6,[12] thus confirming the applicability of the PAM to TKI. We also find that this STI phase is in the vicinity of an insulator–metal transition driven by the enhancement of V.

In heavy-fermion systems, the interplay and competition between Kondo screening and magnetic correlation can motivate magnetic transitions when the Kondo interaction is reduced.[13] Similarly, in a half-filled TKI, theoretical calculations have verified a transition to the AF phase when the hybridization interaction V is weakened,[10,14] which is reminiscent of the induced magnetism in pressurized SmB_6.[15–17] Moreover, our earlier work has proved that due to the combined $\mathcal{S}$ TRS and translation operations, the AF states in the TKI remain topologically distinguishable, regardless of the breaking of TRS by magnetic order. We developed a $\mathcal{Z}_2$ topological classification for the AF states in the TKI, and proposed a novel AFTI phase under a unique setting of model parameters, together with an AFTI–nontopological AF insulator (nAFI) transition while EH was shifted in some

*Supported by the National Natural Science Foundation of China under Grant Nos 11764010, 11504061, 11564008, 11704084, and 11704166, the Natural Science Foundation of Guangxi Province under Grant Nos 2017GXNSFAA198169 and 2017GXNSFBA198115, and the SPC-Lab Research Fund under Grant No XKFZ201605.

**Corresponding author. Email: lihuan@glut.edu.cn; zhengxiaojun323@foxmail.com

© 2018 Chinese Physical Society and IOP Publishing Ltd

way.[10] Unfortunately, why the AFTI should appear in such a parameter region is still unclear, and it remains unclear whether new AF phases exist in other parameter regions. We have shown that at least near the magnetic boundary (MB), the $\mathcal{Z}_2$ index for AF directly relies on that of the TI phase from which the AF order develops.[10] Therefore, to investigate all possible AF phases with distinct topologies, the magnetic transition and classification of AF phases should be discussed on the basis of the PM phase diagrams summarizing all TIs, i.e. the four STIs and two WTIs should be properly included to study the AF transition as well as the topological transitions between AF phases.

We use the spin-1/2 PAM to characterize the 3D TKI in a cubic lattice[18]

$$H = H_d + H_f + H_{\rm df} + H_U, \tag{1}$$

where $H_d = \sum_{\boldsymbol{k},\alpha}(\epsilon^d_{\boldsymbol{k}} - \mu)d^\dagger_{\boldsymbol{k}\alpha}d_{\boldsymbol{k}\alpha}$, $H_f = \sum_{\boldsymbol{k},\alpha}(\epsilon_f + \epsilon^f_{\boldsymbol{k}} - \mu)f^\dagger_{\boldsymbol{k}\alpha}f_{\boldsymbol{k}\alpha}$, and $H_{\rm df} = V\sum_{\boldsymbol{k},\alpha,\beta}\boldsymbol{S}_{\boldsymbol{k}}\cdot\boldsymbol{\sigma}_{\alpha\beta}d^\dagger_{\boldsymbol{k}\alpha}f_{\boldsymbol{k}\beta} +$ H.c. is the Kondo hybridization with spin-orbit coupling, in which $\boldsymbol{S}_{\boldsymbol{k}} = (\sin\boldsymbol{k}\cdot\boldsymbol{a}_1, \sin\boldsymbol{k}\cdot\boldsymbol{a}_2, \sin\boldsymbol{k}\cdot\boldsymbol{a}_3)$,[18] with the element vectors $\boldsymbol{a}_1$, $\boldsymbol{a}_2$, and $\boldsymbol{a}_3$ for the cubic lattice. $H_U = U\sum_i n^f_{i\uparrow}n^f_{i\downarrow}$ is the on-site Coulomb repulsion between f electrons, and we consider infinite U in this work. We includes EH up to the third neighbors, with $t_{d(f)}$, $t'_{d(f)}$, and $t''_{d(f)}$ denoting the nearest-neighbor, next-nearest-neighbor, and next-next-nearest-neighbor hopping amplitudes, respectively; these which determine the tight-binding dispersions $\epsilon^{d(f)}_{\boldsymbol{k}}$. The chemical potential μ is used to fix the total electron number to half filling $n_t = 2$. The variable EH, hybridization interaction V, and f energy level ϵ_f are considered. In what follows, $t_d = 1$ is set as energy units, and we choose $t_f = -0.2$ and keep $t'_d/t_d = t'_f/t_f$ to obtain a medium gapped insulating phase (unless the insulator–metal transition is discussed).

We employ the Kotliar–Ruckenstein (K–R) slave-boson method[10,19,20] to solve the PAM. Similar to Coleman's slave boson theory,[18] the mean-field approximation of the PAM's Eq. (1) in large-U limit reads[10]

$$H_{\rm MF} = N(-\eta n_f) + \sum_{\boldsymbol{k},\alpha,\beta}(d^\dagger_{\boldsymbol{k}\alpha}, f^\dagger_{\boldsymbol{k}\alpha}) \cdot \begin{pmatrix} (\epsilon^d_{\boldsymbol{k}} - \mu)\delta_{\alpha\beta} & \tilde{V}\boldsymbol{S}_{\boldsymbol{k}}\cdot\vec{\sigma}_{\alpha\beta} \\ \tilde{V}\boldsymbol{S}_{\boldsymbol{k}}\cdot\vec{\sigma}_{\alpha\beta} & (\tilde{\epsilon}^f_{\boldsymbol{k}} - \mu)\delta_{\alpha\beta} \end{pmatrix}\begin{pmatrix} d_{\boldsymbol{k}\beta} \\ f_{\boldsymbol{k}\beta} \end{pmatrix}, \tag{2}$$

where the effective hybridization $\tilde{V} = VZ$ is renormalized by factor $Z = \sqrt{2(1-n_f)/(2-n_f)}$, and the effective f dispersion $\tilde{\epsilon}^f_{\boldsymbol{k}} = \epsilon_f + \eta + Z^2\epsilon^f_{\boldsymbol{k}}$, in which η shifts the f level, n_f is the density of f electrons per site, and N is the number of lattice sites. The PM mean field parameters n_f, η, and μ are solvable through saddle-point solutions for $H_{\rm MF}$. Then, the quasiparticle dispersions, which are the eigenvalues of the Hamiltonian matrix in Eq. (2) (in a modified form), are used to identify the $\mathcal{Z}_2$ index.

Table 1. Parameters and $\mathcal{Z}_2$ invariants of the TI phases shown in Fig. 1. In all phases $t_f = -0.2$.

Phase	t'_d	t''_d	t'_f	t''_f	ϵ_f	V	δ_Γ	δ_X	δ_M	δ_R	ν_0	ν_j	Dirac points[a]
$\mathrm{STI}_{\bar{\Gamma}}$	0.26	0.26	−0.052	−0.052	−2	0.7	1	−1	−1	−1	1		$\bar{\Gamma}$
$\mathrm{STI}_{\bar{\Gamma}\bar{X}}$	−0.35	−0.35	0.07	0.07	−2	1	−1	1	−1	−1	1		$\bar{\Gamma}$, $\bar{X}$
$\mathrm{STI}_{\bar{M}}$	0.252	0.252	−0.0504	−0.0504	−2	1.5	1	1	1	−1	1		$\bar{M}$
$\mathrm{STI}_{\bar{M}\bar{X}}$	0.4	0	−0.08	0	−1	1	1	1	−1	1	1		$\bar{M}$, $\bar{X}$
$\mathrm{WTI}_{\bar{\Gamma}\bar{M}}$	−0.6	0	0.12	0	−1	1	−1	1	1	−1	0	1	$\bar{\Gamma}$, $\bar{M}$
$\mathrm{WTI}_{\bar{X}}$	−0.2	0	0.04	0	−2	1	1	1	−1	−1	0	1	$\bar{X}$

[a]The surface dispersions are calculated on the (001) surface.

In the last two rows of Fig. 1, we show six types of distinct quasiparticle spectra of PM TIs, each with different model parameters listed in Table 1 and compared with d and f dispersions. At the eight high symmetry points (HSPs) $\boldsymbol{k}_m$ in the 3D Brillouin zone (BZ) (i.e. $\Gamma = (0,0,0)$; $X = (\pi,0,0)$, $(0,\pi,0)$, $(0,0,\pi)$; $M = (\pi,\pi,0)$, $(\pi,0,\pi)$, $(0,\pi,\pi)$; and $R = (\pi,\pi,\pi)$), the hybridization vanishes (due to its odd parity). Consequently, the quasiparticle energy equals either $\epsilon^d_{\boldsymbol{k}}$ or $\tilde{\epsilon}^f_{\boldsymbol{k}}$, leading to the parity of occupied states $\delta_m = 1$ or -1 at $\boldsymbol{k}_m$, respectively. Therefore, the strong topological index ν_0 can be easily obtained by observing the bulk dispersions in Fig. 1 via $(-1)^{\nu_0} = \prod_{m\in\mathrm{HSP_s}}\delta_m$. Meanwhile, the weak topological indices ν_j $(j = x,y,z)$ are calculated from the HSPs on k_j plane P_j through $(-1)^{\nu_j} = \prod_{m\in P_j}\delta_m$.[6] The δ_m and $\mathcal{Z}_2$ indices for six TIs are listed in Table 1.

By diagonalizing 40 slabs to simulate the 3D lattice with an opened (001) surface, the surface states of the six TIs are computed and displayed in the second and third rows of Fig. 1. On the (001) surface, there are four HSPs: $\bar{\Gamma} = (0,0)$; $\bar{X} = (\pi,0)$, $(0,\pi)$; and $\bar{M} = (\pi,\pi)$. Each of the six TIs in Fig. 1 has Dirac points located at different HSPs. The requirement of an odd number of Dirac points on the surface of the STI leads to four inequivalent STIs, $\mathrm{STI}_{\bar{\Gamma}}$, $\mathrm{STI}_{\bar{M}}$, $\mathrm{STI}_{\bar{\Gamma}\bar{X}}$, and $\mathrm{STI}_{\bar{M}\bar{X}}$, in which the subscripts denote the locations of the Dirac points. For WTIs, there are an even number of Dirac points, resulting in two WTIs: $\mathrm{WTI}_{\bar{\Gamma}\bar{M}}$ and $\mathrm{WTI}_{\bar{X}}$. For the nKI, generally no Dirac point exists; however, there is a special nKI with Dirac points at all four HSPs, since the Fermi level crosses its surface states an even number of times between two arbitrary HSPs. This phase is actually a non-topological phase rather than a topological one.

In the first row of Fig. 1, with varying t'_d, ϵ_f, and

V, we locate the topological boundaries among all possible TIs, which are determined by the change in the $\mathcal{Z}_2$ index. The topological transitions between TIs are generated by closing and reopening the insulating gap at a certain HSP, leading to an inversion of parity and consequently the shifting of the $\mathcal{Z}_2$ index.[10]

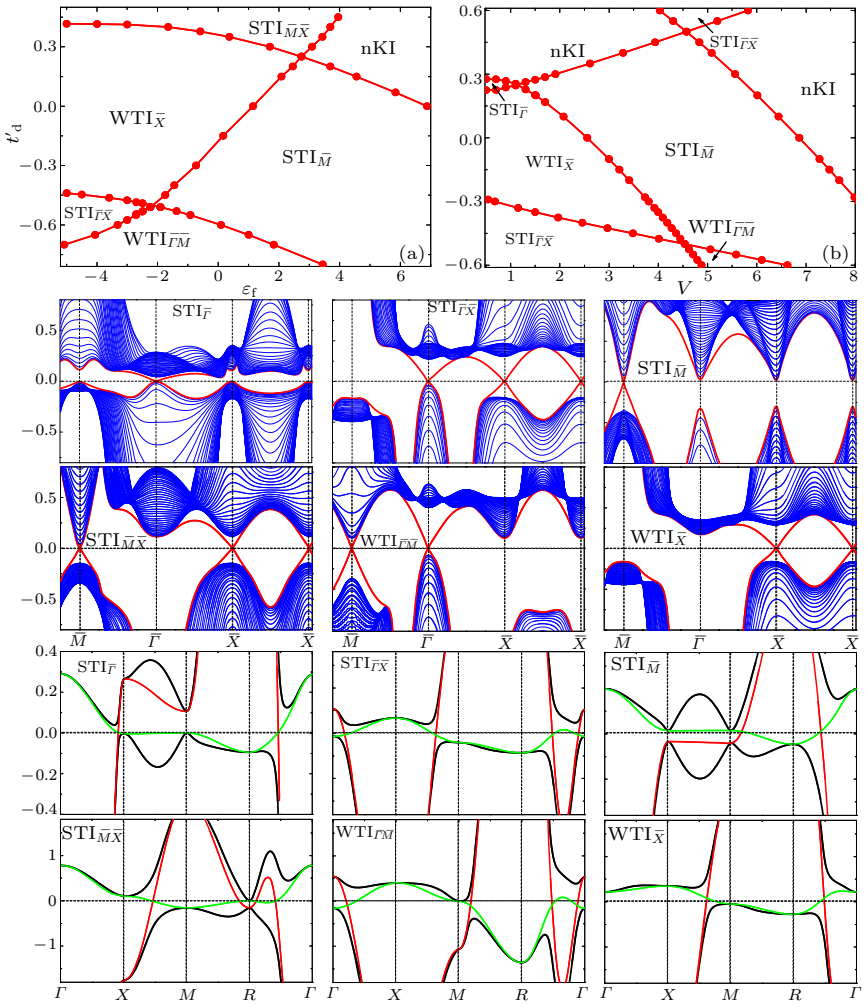

Fig. 1. First row: PM phase diagrams of the 3D TKI. Parameters: $t_f = -0.2$, $t'_f/t_f = t'_d/t_d$, (a) $V = 1$, $t''_d = t''_f = 0$; (b) $\epsilon_f = -2$, $t''_d = t'_d$, $t''_f = t'_f$. Second and third rows: slab dispersions of TIs. The red lines denote the surface states. Last two rows: quasiparticle dispersions (black solid lines) in six TIs; the red and green lines are d- and renormalized f-dispersions, respectively. Parameters and $\mathcal{Z}_2$ invariants for each TI are listed in Table 1.

So far, we have set $t'_f/t_f = t'_d/t_d$, under which the Dirac points in TIs all cross the Fermi energy, leading to the vanishing of the Fermi surface. For TKI candidate SmB_6, medium-sized surface Fermi rings around $\bar{\Gamma}$ and $\bar{X}$ were detected through ARPES, verifying an STI$_{\bar{\Gamma}\bar{X}}$ phase.[12] Although our study of TKI is based on the simplified PAM, it can still produce an STI$_{\bar{\Gamma}\bar{X}}$ with similar surface states as SmB_6. To carry this out, we chose EH departing from $t'_f/t_f = t'_d/t_d$, and found an STI$_{\bar{\Gamma}\bar{X}}$ phase with Fermi surfaces and helical spin textures quite similar to SmB_6 (see Figs. 2(c) and 2(d)). Furthermore, this phase is in the vicinity of an insulator–metal transition generated by shifting V or ϵ_f (see Figs. 2(a) and 2(b)), which may account for the metallic phase observed in pressurized SmB_6.[15,21]

Based on the PM phase diagrams of TIs, we now study the AF transitions in the TKI. In our previous work, the original K–R method of the symmetric PAM[19,20] was generalized to treat AF phases in the non-symmetric case,[10] which can be applied to the TKI. The resulting mean-field Hamiltonian is rather complicated in that in addition to n_f, η, and μ, two AF order parameters m_f and h should be determined. Moreover, two renormalization factors Z_1 and Z_2 arise. Due to the $\mathcal{S}$ symmetry combined by TRS and lattice translation, the AF phases in the TKI fall into the $\mathcal{Z}_2$ topological class, and the $\mathcal{Z}_2$ index ν is calculated from the parities of the occupied spectra at four Kramers degeneracy momenta (KDM) $\boldsymbol{p}_m$ (Γ and three X points) via $(-1)^\nu = \prod_{\boldsymbol{p}_m \in \mathrm{KDM}} \delta_m$, in which $\delta_m = \prod_i \xi_i(\boldsymbol{p}_m)$, with the parity $\xi_i(\boldsymbol{p}_m)$ of the ith occupied state at $\boldsymbol{p}_m$ equaling either 1 or -1 when the quasiparticle energy equals that of d or f at $\boldsymbol{p}_m$, respectively.[10] Particularly, the strong topological index ν_0 on the PM side of the MB directly determines ν of the AF phase near the MB, namely, $\nu_0 = 1$ (STI)

leads to $\nu = 1$ (AFTI), while $\nu_0 = 0$ (WTI or nKI) leads to $\nu = 0$ (nAFI),[7,10] giving a straightforward verification of the AF phases near the MB.

The magnetic critical hybridization V_c is calculated as a function of t'_d, and then the MB plotted by V_c is added to the phase diagram (see Fig. 3). The MB crosses the topological boundaries of TIs in two parts: one near $t'_d = 0.25$, and the other around $t'_d = -0.35$ (see the insets of Fig. 3 for details).

Around $t'_d = -0.35$ the MB is divided by the $\mathrm{STI}_{\bar{\Gamma}\bar{X}}$–$\mathrm{WTI}_{\bar{X}}$ transition line into two parts, leading to the AFTI and nAFI just below the two parts of the MB, respectively. However, when V is lowered further from the MB, ν of AF phases should be computed from the 3D spectra (e.g. see Figs. 4(b) and 4(d)) to determine the AFTI–nAFI topological boundary, which is demonstrated by the green line near $t'_d = -0.35$ in Fig. 3. The AFTI–nAFI transition is realized via parity inversion during gap closing and reopening at Γ, and it converges with the $\mathrm{STI}_{\bar{\Gamma}\bar{X}}$–$\mathrm{WTI}_{\bar{X}}$ boundary at the MB (see the lower inset in Fig. 3).

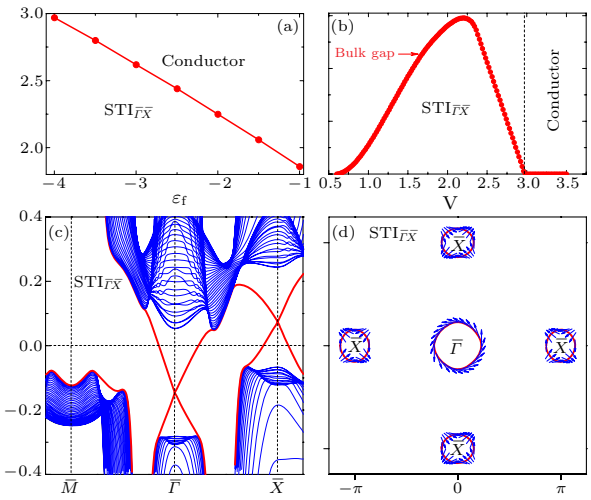

Fig. 2. (a) Insulator–metal transition from the $\mathrm{STI}_{\bar{\Gamma}\bar{X}}$ to the conducting phase. (b) Closing of bulk gap during this transition. (c) Slab dispersions of $\mathrm{STI}_{\bar{\Gamma}\bar{X}}$. (d) Surface Fermi rings and spin textures of $\mathrm{STI}_{\bar{\Gamma}\bar{X}}$. Here $t'_d = t''_d = -0.375$, $t_f = -0.23$, and $t'_f = t''_f = 0.2$; $\epsilon_f = -4$ for (b) to (d), and $V = 1$ for (c) and (d).

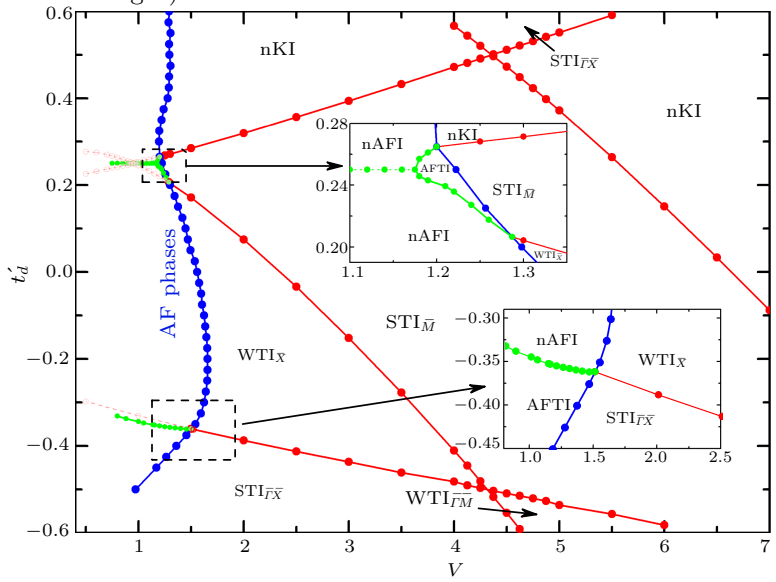

Fig. 3. MB in the 3D TKI (blue lines). Near $t'_d = 0.25$ and -0.35 topological transitions between AF phases take place (green solid lines). Parameters: $\epsilon_f = -1.5$, $t''_d = t'_d$, $t''_f = t'_f$, $t_f = -0.2$, and $t'_f/t_f = t'_d/t_d$.

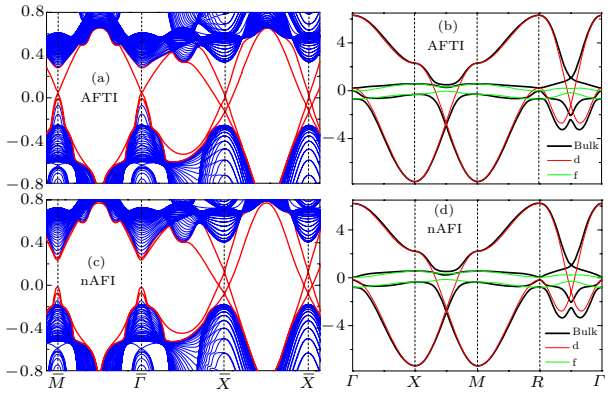

Fig. 4. Surface dispersions (left) and quasiparticle dispersions (right) of the AFTI and nAFI near the AF topological boundary in the lower inset of Fig. 3. Here, $V = 1.4$, $t'_d = -0.37$ for the AFTI, and $t'_d = -0.35$ for the nAFI.

Near $t'_d = 0.25$, the MB is separated by $\mathrm{WTI}_{\bar{X}}$–$\mathrm{STI}_{\bar{M}}$ and $\mathrm{STI}_{\bar{M}}$–nKI lines into three parts. Below the middle part of the MB (which touches $\mathrm{STI}_{\bar{M}}$), an AFTI arises; meanwhile, below the other two parts of the MB, the nAFI emerges. The AFTI–nAFI transition forms a narrow waterdrop-shaped area in which the AFTI survives (green solid line in the upper inset in Fig. 3). Furthermore, although nAFIs above and below $t'_d = 0.25$ have quite different dispersions (compare Fig. 5(b) with 5(f)), they still have equal $\nu = 0$ since their magnetic orders grow from the nKI and WTI, respectively. Although the band gap is closed at the boundary between two nAFIs, no parity inversion occurs, and consequently no topological transition takes place (see the green dashed line in the upper inset of Fig. 3).

The surface states of AF phases are shown in Figs. 4(a) and 4(c) near $t'_d = -0.35$, and in Figs. 5(a), 5(c), and 5(e) around $t'_d = 0.25$, respectively. In AFTIs, the Dirac points at $\bar{\Gamma}$ and $\bar{M}$ protected by topology are robust (see Figs. 4(a) and 5(c)). Furthermore, the Dirac surface states of two AFTIs (one near $\mathrm{STI}_{\bar{M}}$ and the other near $\mathrm{STI}_{\bar{\Gamma}\bar{X}}$) disperse quite differently; the former constructs a valley shape (figure 5(c)). In contrast, the gapless surface states at $\bar{X}$ in both the AFTI and nAFI (figures 4(a), 4(c), and 5(a)) are not robust since they can be gapped by an additional factor such as gate voltage.[10]

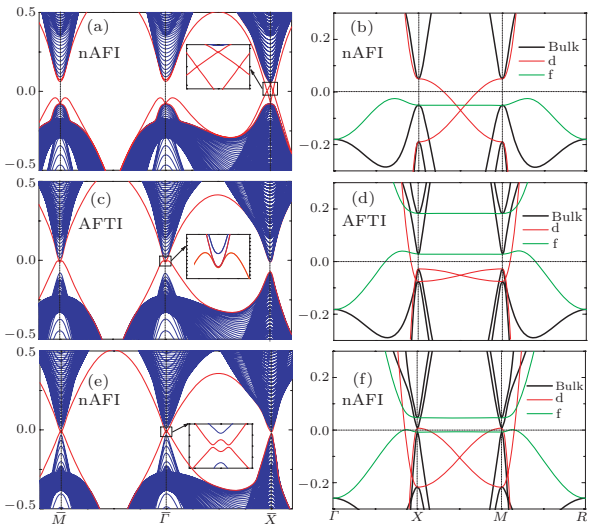

Fig. 5. Surface spectra (left) and quasiparticle dispersions (right) of the three AF phases near the AF topological boundary in the upper inset of Fig. 3. $V = 1.19$. For top, middle, and bottom rows, $t'_d = 0.235$, 0.253, and 0.264, respectively.

In summary, we performed a slave-boson mean-field analysis of the 3D TKI using a spin-orbit coupled PAM, and presented the phase diagrams including all possible PM TIs in the TKI: four STIs and two WTIs, each with distinguishable locations of Dirac points. We also obtained an $\mathrm{STI}_{\bar{\Gamma}\bar{X}}$ phase with similar surface states as SmB_6, and found that it can be driven to a conducting state through an insulator–metal transition by enhanced hybridization. We also investigated the MB of AF phases in the TKI, and found the topological transitions between the AFTI and nAFI in two narrow regions in parameter space. Moreover, we found two types of AFTIs with distinct dispersions at the Dirac points. Although our work was based on an uniform mean-field approximation, any site-dependent treatment will not break the application of $\mathcal{Z}_2$ classification of both PM and AF states.[14,17] We hope that our work can help us reach a comprehensive understanding of novel AFTI phases in strongly correlated electron systems.

References

[1] Qi X L and Zhang S C 2011 *Rev. Mod. Phys.* **83** 1057
[2] Go A, Witczak-Krempa W, Jeon G S, Park K and Kim Y B 2012 *Phys. Rev. Lett.* **109** 066401
[3] Yu S L, Xie X C and Li J X 2011 *Phys. Rev. Lett.* **107** 010401
[4] Wang Z and Zhang S C 2012 *Phys. Rev.* B **86** 165116
[5] Wan X G, Turner A M, Vishwanath A and Savrasov S Y 2011 *Phys. Rev.* B **83** 205101
[6] Dzero M, Sun K, Coleman P and Galitski V 2012 *Phys. Rev.* B **85** 045130
[7] Mong R S K, Essin A M and Moore J E 2010 *Phys. Rev.* B **81** 245209
[8] Fang C, Gilbert M J and Bernevig B A 2013 *Phys. Rev.* B **88** 085406
[9] Li Z, Su H, Yang X and Zhang J 2015 *Phys. Rev.* B **91** 235128
[10] Li H, Zhong Y, Liu Y, Luo H G and Song H F 2018 *J. Phys.: Condens. Matter* **30** 435601
[11] Legner M, Rüegg A and Sigrist M 2014 *Phys. Rev.* B **89** 085110
[12] Xu N, Ding H and Shi M 2016 *J. Phys.: Condens. Matter* **28** 363001
[13] Vekić M, Cannon J W, Scalapino D J, Scalettar R T and Sugar R L 1995 *Phys. Rev. Lett.* **74** 2367
[14] Peters R, Yoshida T and Kawakami N 2018 *Phys. Rev.* B **98** 075104
[15] Zhou Y Z, Wu Q, Rosa P F S, Yu R, Guo J, Yi W, Zhang S, Wang Z, Wang H H, Cai S, Yang K, Li A, Jiang Z, Zhang S, Wei X J, Huang Y Y, Sun P J, Yang Y F, Fisk Z, Si Q M, Zhao Z X and Sun L L 2017 *Sci. Bull.* **62** 1439
[16] Butch N P, Paglione J, Chow P, Xiao Y, Marianetti C A, Booth C H and Jeffries J R 2016 *Phys. Rev. Lett.* **116** 156401
[17] Chang K W and Chen P J 2018 *Phys. Rev.* B **97** 195145
[18] Alexandrov V, Coleman P and Erten O 2015 *Phys. Rev. Lett.* **114** 177202
[19] Kotliar G and Ruckenstein A E 1986 *Phys. Rev. Lett.* **57** 1362
[20] Sun S J, Yang M F and Hong T M 1993 *Phys. Rev.* B **48** 16127
[21] Paraskevas P, Martin B and Mohamed M 2015 *Europhys. Lett.* **110** 66002